MJO in the NCAR CAM2 with the Tiedtke Convective Scheme*

PING LIU AND BIN WANG

International Pacific Research Center, SOEST, University of Hawaii at Manoa, Honolulu, Hawaii

KENNETH R. SPERBER

Program for Climate Model Diagnosis and Intercomparison, Lawrence Livermore National Laboratory, Livermore, California

TIM LI

International Pacific Research Center, SOEST, University of Hawaii at Manoa, Honolulu, Hawaii

GERALD A. MEEHL

National Center for Atmospheric Research, Boulder, Colorado

(Manuscript received 11 August 2004, in final form 11 January 2005)

ABSTRACT

The boreal winter Madden–Julian oscillation (MJO) remains very weak and irregular in the National Center for Atmospheric Research (NCAR) Community Atmosphere Model version 2 (CAM2) as in its direct predecessor, the Community Climate Model version 3 (CCM3). The standard version of CAM2 uses the deep convective scheme of Zhang and McFarlane, as in CCM3, with the closure dependent on convective available potential energy (CAPE). Here, sensitivity tests using several versions of the Tiedtke convective scheme are conducted. Typically, the Tiedtke convection scheme gives an improved mean state, intraseasonal variability, space–time power spectra, and eastward propagation compared to the standard version of the model. Coherent eastward propagation of MJO-related precipitation is also much improved, particularly over the Indian–western Pacific Oceans. A composite life cycle of the model MJO indicates that over the Indian Ocean wind-induced surface heat exchange (WISHE) functions, while over the western/central Pacific Ocean aspects of frictional moisture convergence are evident in the maintenance and eastward propagation of the oscillation.

1. Introduction

The Madden–Julian oscillation (MJO; Madden and Julian 1971, 1972) is the dominant mode of intraseasonal variability and considered to play an important role in time- and space-scale interactions in the climate system (Meehl et al. 2001). Characteristic features of the MJO include power spectra dominated by periods of 30–70 days and zonal wavenumbers 1–3, stronger eastward than westward propagation, out-of-phase structure of 850- and 200-hPa wind, and larger amplitude during boreal winter than summer (Madden and Julian 1994; Hendon and Salby 1994). A mixed Kelvin–Rossby wave structure is characteristic over the Indian and western Pacific Oceans, where the circulation is strongly coupled to convection (e.g., Rui and Wang 1990; Chao and Lin 1994). The oscillation has a Kelvin wave structure with more rapid eastward propagation in regions away from the main convection.

The evolution and eastward propagation of the MJO involve complicated interactions among large-scale circulations, tropical planetary waves, boundary layer moisture supply, transport and phase change of water vapor, and the associated latent heat release (Meehl et al. 1996). Observations indicate that low-level moisture convergence occurs to the east of the main MJO convection as a consequence of boundary layer friction (Hendon and Salby 1994; Salby and Hendon 1994; Jones and Weare 1996; Maloney and Hartmann 1998,

* International Pacific Research Center Contribution Number 319 and School of Ocean and Earth Science and Technology Contribution Number 6572.

Corresponding author address: Dr. Ping Liu, POST 409J, International Pacific Research Center, SOEST, University of Hawaii at Manoa, 1680 East–West Road, Honolulu, HI 96822.
E-mail: pliu@hawaii.edu

hereafter MH98; Woolnough et al. 2000; Sperber 2003). Through this quadrature relationship, it is believed that low-level moisture convergence preconditions the atmosphere through the buildup of moist static energy such that it promotes the development of the deep convection associated with the MJO (Hendon and Liebmann 1990; Bladé and Hartmann 1993; Hu and Randall 1994; MH98; Maloney and Hartmann 2001).

Global atmospheric general circulation models (AGCMs) have a wide range of ability in simulating the observed MJO features (e.g., Park et al. 1990; Slingo et al. 1996). Many models can reproduce stronger eastward- than westward-propagating equatorial zonal wind signals, but coherent propagation of convection is less well simulated. Most AGCMs analyzed by Park et al. (1990) and Slingo et al. (1996) produce intraseasonal signals with higher-than-observed phase speeds in convective regions, periods that are too short (<30 days), amplitudes smaller than observed, and little apparent seasonality of the MJO signals. Slingo et al. (1996) further suggested that AGCMs having a better mean state tend to produce a more realistic MJO, which is supported by recent studies with coupled GCMs (Gualdi et al. 1999; Hendon 2000; Kemball-Cook et al. 2002; Inness and Slingo 2003; Inness et al. 2003).

Convective parameterizations implemented in an AGCM play a key role in simulating a reasonable MJO (Inness and Gregory 1997; Wang and Schlesinger 1999; Maloney and Hartmann 2001). Based on comparison of various cumulus parameterizations in *different* models, Slingo et al. (1996) suggested that convective schemes closed on buoyancy tend to produce better MJO signals than those closed on moisture convergence. Other studies using a *single* model with different cumulus schemes (Chao and Deng 1998; Wang and Schlesinger 1999; Lee et al. 2003) show that the moist convective adjustment (MCA; Manabe et al. 1965) scheme produces the strongest MJO variability, the modified Arakawa–Schubert (AS) scheme (Arakawa and Schubert 1974) the weakest, and the Kuo (1974) scheme intermediate in behavior. Wang and Schlesinger (1999) found that, as the relative humidity criterion (RHC) for convection increases, the simulated MJO becomes stronger for these three schemes. However, Maloney and Hartmann (2001) found that the MJO in the National Center for Atmospheric Research (NCAR) Community Climate Model version 3.6 (CCM3: Kiehl et al. 1998) with the relaxed AS scheme is not improved by increasing the RHC. They also showed that the MJO is highly sensitive to the parameterization of the evaporation of convective precipitation in unsaturated environmental air and saturated downdrafts. These diverse results suggest that further study of the sensitivity of the MJO simulation to the convective scheme employed and the details of how it is tuned is necessary.

Maloney and Hartmann (2001) and Maloney (2002) found that the standard CCM3 employing the deep convection parameterization of Zhang and McFarlane (1995; hereafter ZM95) produced an MJO signal in zonal winds and precipitation with an amplitude much weaker than observed. A weak MJO is also produced in the Canadian Climate Center GCM with the same deep convective scheme (Sheng 1995). As shown by Maloney and Hartmann (2001) and Maloney (2002), the MJO in the CCM3 was markedly improved by implementing the relaxed Arakawa–Schubert (McRAS) scheme of Moorthi and Suarez (1992) as modified by Sud and Walker (1999). Intraseasonal zonal wind variability was enhanced and eastward phase speed was realistic. A coherent precipitation signal was generated, particularly over the western Pacific warm pool. However, CCM3 with McRAS had some deficiencies, especially over the Indian Ocean where the simulation of convection and wind anomalies was notably weaker than observed. Although the frictional moisture convergence mechanism was present, precipitation was in phase with low-level convergence, different from the quadrature relationship observed. Sensitivity experiments (Maloney 2002) showed that the wind-induced surface heat exchange (WISHE: Emanuel 1987; Neelin et al. 1987) mechanism could not explain the coincidence of convection with 850-hPa easterly anomalies. Removing WISHE produced an even more robust MJO.

The fifth generation of the NCAR AGCM, the Community Atmosphere Model version 2 (CAM2), is a descendent of the CCM3. The major changes in CAM2 relative to CCM3 are listed in section 2. It is noteworthy here that the CAM2 retains the ZM95 scheme for parameterization of deep convection. Consistent with the analysis of Sperber (2004), we will show that this model does not represent the MJO.

The intent of this study is to 1) improve the MJO simulation in the CAM2 by implementing the Tiedtke (1989) convective scheme that is closed on moisture convergence, 2) test the sensitivity of the MJO simulation by using the convective available potential energy (CAPE) closure of Nordeng (1994) for deep convection in the Tiedtke (1989) scheme, and 3) assess the WISHE and frictional moisture convergence mechanisms in the life cycle of the simulated MJO.

Section 2 introduces the CAM2; provides an overview of the Tiedtke (1989) scheme and its revision by Nordeng (1994); and describes observational data, experimental design, and procedure for data analysis. Section 3 presents the simulated mean state and basic MJO features. Section 4 gives the composite life cycle of the

TABLE 1. Conventions for the integrations using the CAM2 incorporated with different convective schemes.

Abbreviations	Deep convective scheme	Shallow/middle convective scheme
CTL	Zhang and McFarlane (1995), closed on CAPE	Hack (1994), closed on CAPE
TN_DD30	Tiedtke (1989) revised by Nordeng (1994), moisture convergence as a first guess of CAPE and closed on CAPE; downdrafts are 30% equivalent updrafts	Tiedtke (1989), closed on moisture convergence
T_DD20	Tiedtke (1989), closed on moisture convergence; downdrafts are 20% equivalent updrafts	Tiedtke (1989), closed on moisture convergence

model MJO. Section 5 summarizes the results and provides discussion, including the caveats of the study.

2. Model, convective schemes, integrations, and observational data

a. The NCAR CAM2

In the present study, we use the CAM2.0.2 version released in July 2003. The horizontal resolution is T42 (approximately 2.8° latitude by 2.8° longitude) with 26 hybrid vertical levels, an increase from 19 levels in the CCM3. A new prognostic scheme parameterizes cloud-condensed water (Zhang et al. 2003; Rasch and Kristjánsson 1998). Over the sea ice, a new thermodynamic package is formulated for computing surface exchange fluxes. In the radiation calculations, geometrical cloud overlap is treated by a new, general, and flexible parameterization. Adjacent cloud layers are maximally overlapped. The General Line-by-Line Atmospheric Transmittance and Radiance Model (GENLN2) is employed for the longwave absorptivity and emissivity of water vapor treatment. Evaporation of convective precipitation following Sundqvist (1988) is incorporated. (A complete description of this model version is available online at http://www.ccsm.ucar.edu/models/atm-cam/docs/description/index.html.)

b. Convective schemes

We ported the convective scheme of Tiedtke (1989), revised by Nordeng (1994) from the ECHAM (Roeckner et al. 1996) AGCM version 4 to the CAM2. Table 1 gives a synopsis of the schemes employed in the various sensitivity experiments. The Tiedtke (1989) convective parameterization is a bulk model based on the mass flux concept. This scheme considers deep, shallow, and midlevel convection. Only one type of convection is allowed to take place each time the scheme is activated. An ensemble of clouds occurring in each type of convection is assumed to consist of updrafts and downdrafts. Updrafts usually have entrainment and detrainment from boundary layer turbulence and organized large-scale advection starting from cloud base at the lifting condensation level. Downdrafts occur at the level of free sinking (LFS) where in-cloud air mixes with environmental air and becomes unstable relative to the environment. The mass flux at LFS is taken as a fraction of the cloud-base mass flux, 20% being assumed in Tiedtke (1989). When the moisture convergence is greater than a limit of boundary layer turbulent moisture flux, convection is activated. Deep or penetrative convection occurs when the column-integrated moisture convergence exceeds the boundary layer moisture flux by 110%, as prescribed in the ECHAM4. The simulated mean state and MJO are not sensitive to this limit unless it is specified far beyond the value currently used. Nordeng (1994) extended the organized entrainment and detrainment in penetrative convection to be related to buoyancy, which may improve the MJO simulation (C. Jacob 2005, personal communication). Shallow convection occurs in a suppressed environment where there is surface turbulent moisture flux, and large-scale moisture convergence can be small or even negative. Large-scale lifting of potentially unstable upper air activates midlevel convection. In the ECHAM4, 30% of the updraft mass flux at the cloud base is assumed to be the value of downdrafts at the level of free sinking, while 20% is used in Tiedtke (1989). Our sensitivity experiments show (not shown) that, when using Tiedtke (1989), enhanced downdrafts (30%) do not change the power spectra of 850-hPa zonal wind and precipitation much in wavenumber–frequency domain (cf. section 3), while they tend to produce an MJO that has more power in periods shorter than 30 days and less power in periods longer than 45 days; also, the eastward propagation is faster in the Pacific Ocean. Consequently, the 20% equivalent downdrafts produce a more reasonable MJO signal than 30% and will be discussed in the following sections. The sensitivity to the closure of deep convection is tested by using the Nordeng (1994) closure in the Tiedtke (1989) scheme. In this case, the cloud-base mass flux is determined by convective instability, and the scheme is closed on CAPE.

The ZM95 scheme is also a bulk model based on the mass flux concept but it only parameterizes deep convection. It assumes that all clouds share the same cloud base where the mass flux solely depends on CAPE. Updrafts and downdrafts are considered for deep con-

vection. Shallow convection is handled by the Hack (1994) scheme.

c. Experimental design and analysis procedure

We run the CAM2 with different convective schemes or the same scheme with different configurations of closure and downdrafts (Table 1). The standard release of the CAM2.0.2 with ZM95 serves as a control (CTL) run. Runs using the Tiedtke convective scheme are all represented by a capital letter T in the abbreviations with the addition of the capital letter N when the Nordeng (1994) revision is used. The double D represents downdrafts and is followed by the percentage employed.

Sixteen-year-long AMIP-type (Gates 1992) runs are conducted. Boundary conditions are observed time-evolving monthly mean sea surface temperature and sea ice provided by the CAM2 standard release. All runs cover 1 January 1978 to 31 March 1995, with the analysis period being 1 January 1979 to 31 December 1994. Monthly mean outputs are used for mean state analysis. Daily mean outputs in winds, surface latent heat flux, precipitation, and moisture are used for the MJO diagnostics. Pentad (5 day) mean data are derived from the daily mean output. By subtracting their long-term means, daily and pentad anomaly series are derived. A 4–16 pentad (20–80 day) bandpass filter is applied to the complete anomaly series without any tapering. Results here are in good agreement with previous studies where each season was separately windowed and tapered before filtering (e.g., Salby and Hendon 1994). November–April (about 180 days) anomaly series are used for an extended winter (winter in short). Power spectra and regression plots are then derived to analyze the modeled MJO features.

d. Observational data

Winds are from the National Centers for Environmental Prediction (NCEP)–NCAR reanalysis project (Kalnay et al. 1996). We compare the simulated precipitation to the pentad-averaged Climate Prediction Center (CPC) Merged Analysis of Precipitation (CMAP; Xie and Arkin 1997). The same filtering procedure for the model output is applied to the observational data.

3. Mean state and MJO in the CAM2 experiments

a. DJFM mean state: 850-hPa zonal wind and precipitation

Since the mean state is important for MJO simulation, we show the mean states in 850-hPa zonal wind and precipitation during the December–March (DJFM) season in the CTL, TN_DD30, and T_DD20 compared to the NCEP–NCAR reanalysis and CMAP rainfall.

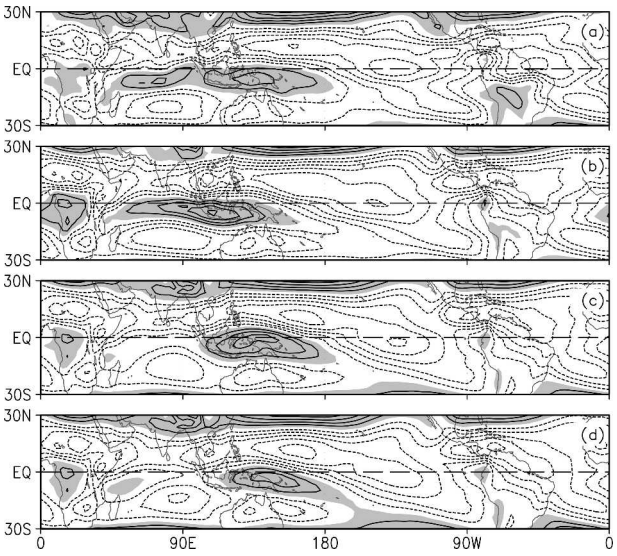

FIG. 1. Long-term (1979–94) mean tropical 850-hPa zonal wind in the DJFM season from (a) the NCEP–NCAR reanalysis, (b) CTL, (c) TN_DD30, and (d) T_DD20. Contour interval is 2 m s^{-1} excluding zero. Regions greater than and equal to zero are shaded.

Figure 1 shows long-term mean (1979–94) 850-hPa zonal wind in the Tropics for the DJFM season. In the reanalysis (Fig. 1a), westerly winds are located over the southern equatorial regions over Africa, the Indian and western Pacific Oceans, and South America. From the Indian Ocean to the central Pacific the westerlies correspond to the location where the eastward propagation of the MJO is prevalent. The CTL run (Fig. 1b) produces westerly winds over the Indian and western Pacific Oceans. Importantly, this westerly patch is centered at 110°E and only extends to 160°E, suggesting that, if eastward propagation of the MJO is present, it will not penetrate as far east as observed. The TN_DD30 simulation (Fig. 1c) fails to represent the westerlies over the tropical Indian Ocean but better simulates their extension to the date line (also seen in the T_DD20) compared to the CTL run. The westerlies over the Indian Ocean are modestly improved in the T_DD20 simulation. Figure 1 indicates that the mean state of the 850-hPa zonal wind is quite sensitive to the convective parameterization. The CAM2 with the Tiedtke (1989) scheme closed on moisture convergence with reduced downdrafts (T_DD20) produces a more realistic mean zonal wind than the Tiedtke scheme closed on CAPE (TN_DD30); although compared to observations and the CTL run, the westerlies over the

Indian Ocean are deficient. The easterly bias occurs in all the CAM2 models with the Tiedtke convective scheme, as presented. This bias is systematic, but the MJO is very different in these model versions, which suggests that the mean state error is not caused by the MJO. However, we cannot conclude that the MJO activities have no feedback to the mean state. Importantly, Inness et al. (2003) have clearly demonstrated that improving the time-mean state results in a better representation of the MJO.

Figure 2 shows the mean state of precipitation in the DJFM season. Similar to CCM3 results from Maloney and Hartmann (2001), the CTL run (Fig. 2b) produces weaker than observed (Fig. 2a) precipitation over the south equatorial Indian and Pacific Oceans. Additionally, precipitation over the South Pacific convergence zone (SPCZ) is about half of that observed. Such a weak mean state in precipitation will be shown to correspond to weak MJO amplitude in these regions. Comparatively, the TN_DD30 (Fig. 2c) precipitation over the SPCZ region is comparable to CMAP, and that over the Indian Ocean is also improved. The T_DD20 (Fig. 2d) produces a precipitation distribution that is closest to CMAP, particularly over the southern Indian and western Pacific Oceans. In the T_DD20 simulation the grid-scale-resolved precipitation over the tropical Indian Ocean and western Pacific makes a larger contribution to the total rainfall than in the other simulations (not shown). This may influence how the model organizes its intraseasonal convection. Despite this improvement in the simulations using the Tiedtke scheme, the rainfall over the Maritime Continent remains underestimated compared to observations. The underestimation of rainfall over the Maritime Continent may be a factor in the poor representation rainfall over the Indian Ocean (Neale and Slingo 2003), while interactions that may give rise to the split intertropical convergence zone over the west Pacific are completely different (Williamson and Olson 2003). Such complexity probably contributes to the difficulty in representing the MJO. The change of mean state can be understood in that convection on different temporal and spatial scales is represented differently by different cumulus schemes. We next explore the relationship of the intraseasonal variance to the mean state.

b. Mean intraseasonal variance of precipitation

Figure 3 shows the 20–80-day bandpass-filtered precipitation variance for the months from November to April. CMAP has variance in excess of 20 mm^2 day^{-2} over the Indian and western Pacific Oceans, with a minimum over the Maritime Continent (Fig. 3a), while the CTL simulation fails to produce variance of this magnitude (Fig. 3b). The runs with the variants of the Tiedtke scheme have more intraseasonal variability, with the T_DD20 overestimating the precipitation variance. When expressed as a percentage of the total variance, improvement using the Tiedtke schemes compared to the CTL scheme is also apparent (Fig. 4). Even so, compared to observations (Fig. 4a) the percent of

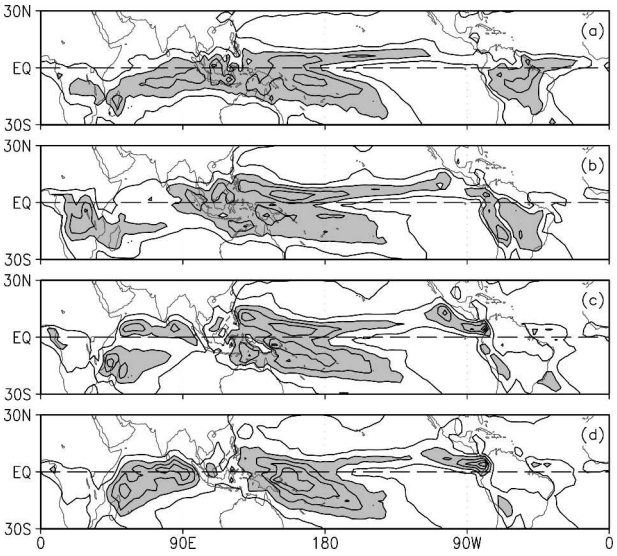

FIG. 2. As in Fig. 1 but for precipitation from (a) CMAP, (b) CTL, (c) TN_DD30, and (d) T_DD20. Contour interval is 3 mm day^{-1}. Regions greater than and equal to 6 mm day^{-1} are shaded.

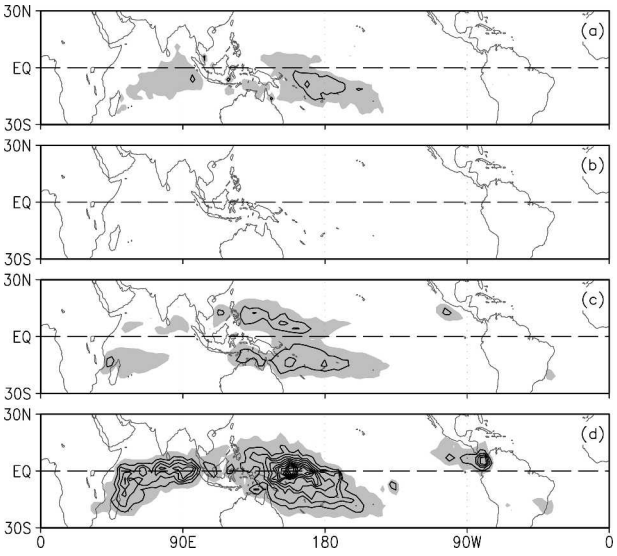

FIG. 3. Mean variance of 20–80-day filtered precipitation in extended winter (180 days from Nov to Apr) from (a) CMAP, (b) CTL, (c) TN_DD30, and (d) T_DD20. Contour starts from 40 with an interval of 20 mm^2 day^{-2}. Regions greater than and equal to 20 mm^2 day^{-2} are shaded.

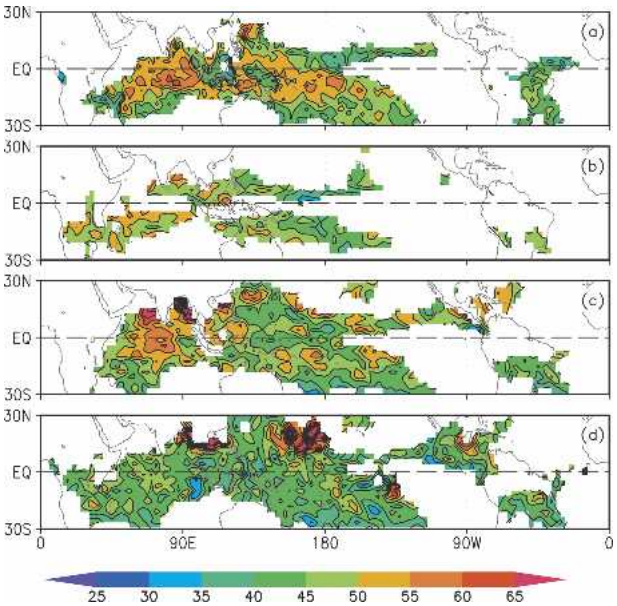

FIG. 4. Mean percentage of 20–80-day filtered to total variance of precipitation in winter from (a) CMAP, (b) CTL, (c) TN_DD30, and (d) T_DD20. Filtered variances equal to and less than 5 mm^2 day^{-2} are omitted.

total variance explained by 20–80-day periods is still underestimated in the Tiedtke sensitivity runs. In the case of T_DD20, both bandpass-filtered (Fig. 4d) and total variance is substantially overestimated compared to observation (not shown).

In summary, the CTL run produced intraseasonal variance that is much smaller than observed in both precipitation and 850-hPa zonal wind (not shown). The Tiedtke scheme closed on CAPE with enhanced downdrafts, TN_DD30, has an improved climatology, but deficiencies remain, particularly over the equatorial Indian Ocean. The scheme closed on moisture convergence and reduced downdrafts, T_DD20, produces a rainfall climatology closer to observations, but with much higher variance in the 20–80-day band for both precipitation (Fig. 3d) and 850-hPa zonal wind (not shown).

c. *Mean power spectra*

The MJO variance shown in Fig. 3 may consist of standing and propagating components, which can be evaluated using wavenumber–frequency analysis. Fourier power spectra of 7°N–7°S averaged 850-hPa zonal wind are calculated using the bandpass-filtered series for each of the 15 winters. The spectra are averaged to obtain the mean power spectrum. As shown in the observational studies (e.g., Hendon and Salby 1994), the MJO propagation dominates the 850-hPa zonal wind and is highly coherent with the convective fields. As seen in Fig. 5a, the observed mean power spectrum is dominated by eastward propagation at zonal wavenumbers 0–3 and periods from 30 to 70 days. The little energy that propagates westward is dominated by wavenumbers 0–2 at a period of 60 days.

The CTL simulation (Fig. 5b) produces a weak power spectrum, consistent with those from CCM3 shown by Maloney and Hartmann (2001). The TN_DD30 (Fig. 5c) run has an improved power spectrum dominated by eastward propagation, with maxima concentrated at zonal wavenumbers 0–3 and periods of 20–70 days. However, the power in the TN_DD30 simulation is only about half that of the reanalysis. The T_DD20 (Fig. 5d) shows the best agreement with the reanalysis, though the eastward power has maxima at 30 and 50 days. This deficiency was found to exist in many earlier AGCMs by Slingo et al. (1996).

Space–time power spectra of precipitation are shown in Fig. 6. The power spectrum from CMAP in Fig. 6a

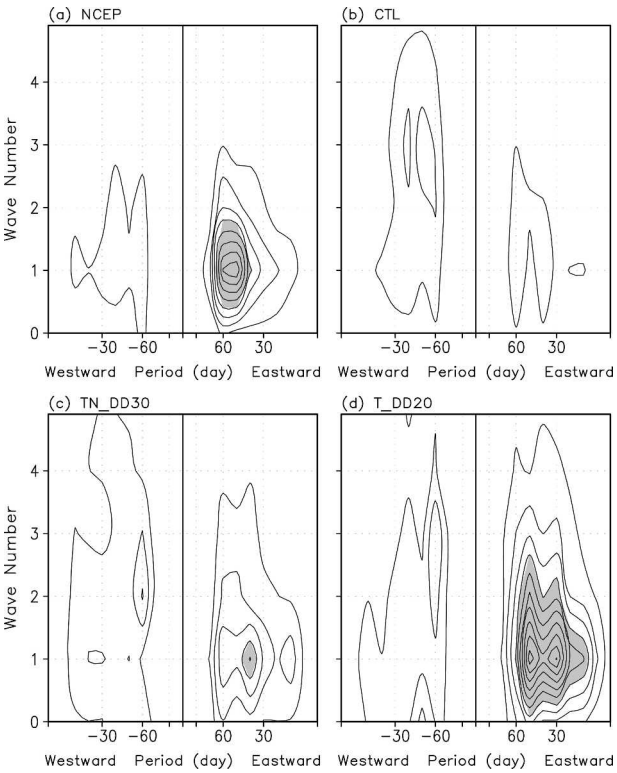

FIG. 5. Mean wavenumber–frequency power spectra in 850-hPa zonal wind in winter. For each season from 1979 to 1994, power spectra are derived from the Fourier coefficients of filtered complete pentad time series averaged between 7°S and 7°N. An average of 15 seasons is derived: from (a) the NCEP–NCAR reanalysis, (b) CTL, (c) TN_DD30, and (d) T_DD20. Contour interval is 2.5 m^2 s^{-2} day. Regions greater than and equal to 10 m^2 s^{-2} day are shaded.

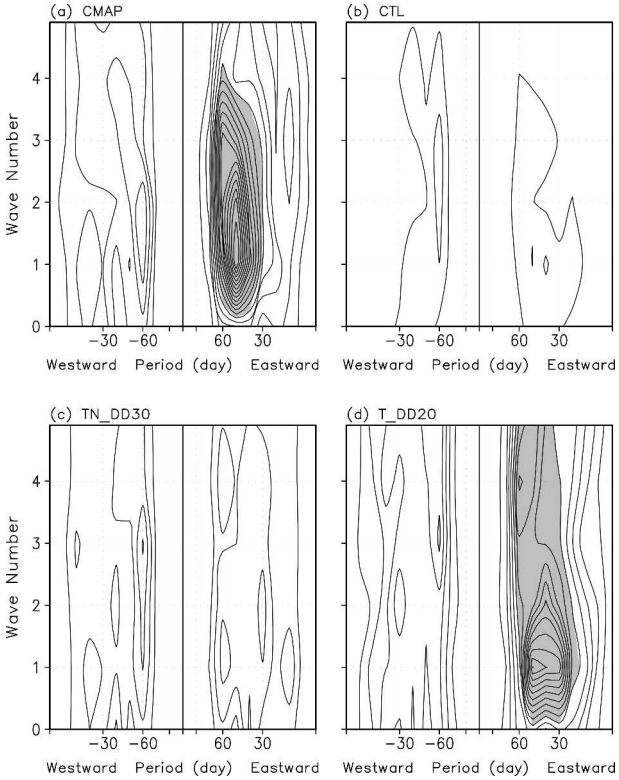

FIG. 6. Mean wavenumber–frequency power spectra in precipitation using the same procedure as in Fig. 5: from (a) CMAP, (b) CTL, (c) TN_DD30, and (d) T_DD20. Contour interval is 1 mm^2 day^{-1}. Regions greater than and equal to 5 mm^2 day^{-1} are shaded.

shows very similar features to that from the 850-hPa zonal wind except for a wider range of dominant zonal wavenumbers. Figure 6b shows that the CTL run has very weak power and lacks dominant eastward propagation, similar to that in the zonal wind in Fig. 5b. Although the TN_DD30 simulation produces stronger MJO power than the CTL in the zonal wind, it does not simulate a commensurate improvement for rainfall (Fig. 6c). The Tiedtke convective scheme closed on moisture convergence (T_DD20; Fig. 6d) produces a more coherent MJO-like power spectrum in precipitation than when closed on CAPE (TN_DD30; Fig. 6c). In the CAM2 framework, a convective scheme closed on static energy or CAPE shows some disadvantages in simulating a realistic spectrum of MJO precipitation. Such a disadvantage is possibly related to the poor simulation of the mean state zonal wind (Fig. 1c) and precipitation (Fig. 2c) and the weak intraseasonal variability over the Indian Ocean (Fig. 3c).

d. Regression with 850-hPa zonal wind

Here we use lagged linear regression to ascertain how well the various simulations represent intraseasonal eastward propagation of the near-equatorial 850-hPa zonal wind. This will enable us to isolate the sensitivity simulation in which a more in-depth analysis should be pursued. Following MH98, we select 155°E as a reference point. Filtered time series are averaged between 10°N and 10°S in the reanalysis and CAM2 experiments. The latitudinal range for averaging is 3° wider here than for the power spectra in Figs. 5 and 6 to extract a more continuous propagating signal in the reanalysis; only a slight difference occurs in the CAM2 runs when using 7°N ~ 7°S. In Fig. 7a the lead–lag correlation in northern winter from the reanalysis shows onset of the MJO in the Indian Ocean at time lags of −30 to −15 days. East of the date line the signal propagates eastward with a faster phase speed relative to that in the Eastern Hemisphere. The period of the oscillation is about 45 days, consistent with the results of Woolnough et al. (2000) and Sperber (2003). The CTL simulation shows virtually no propagating signal (Fig. 7b), consistent with the CAM2 analysis by Sperber (2004) and the CCM3 investigation of Maloney and Hartmann (2001). Figures 7c and 7d indicate that the

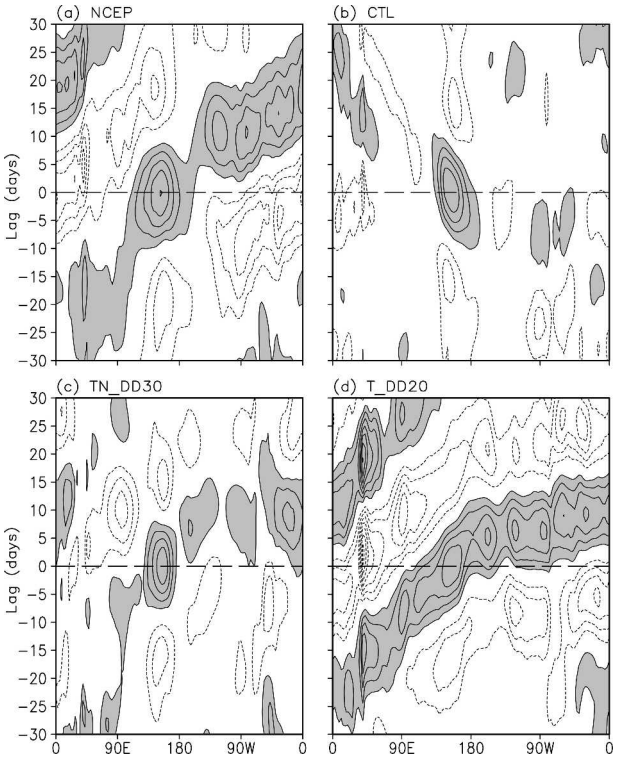

FIG. 7. Average lag correlation coefficients with filtered daily 850-hPa zonal wind in winter averaged 10°S ~ 10°N around the equator: from (a) the NCAP–NCEP reanalysis, (b) CTL, (c) TN_DD30, and (d) T_DD20. Contour interval is 0.2 m s^{-1} excluding zero. Regions greater than and equal to 0.2 m s^{-1} are shaded.

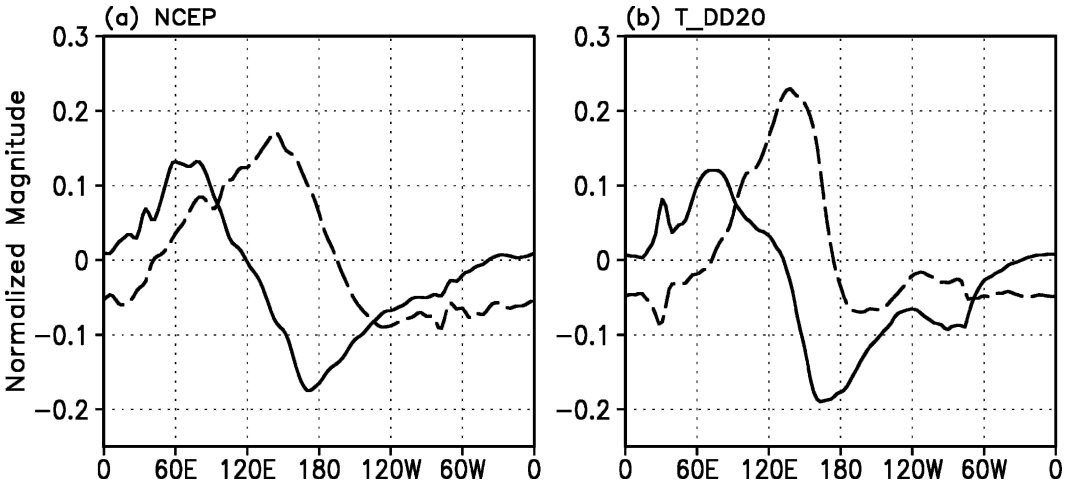

FIG. 8. Spatial distributions of the EOF-1 (solid) and EOF-2 (dashed) calculated from the filtered pentad 850-hPa zonal wind series during the extended winters from 1979 to 1993 (540 pentads in total) around the equator averaged between 7°N and 7°S in (a) the NCEP–NCAR reanalysis and (b) T_DD20. Explanation variance for (a) EOF-1 is 31.9% and EOF-2 is 23.1%, and (b) EOF-1 is 29.4% and EOF-2 is 18.3%.

variants of the Tiedtke scheme give rise to eastward-propagating intraseasonal variability. That closed on moisture convergence, T_DD20 (Fig. 7d), gives an excellent representation of the variations of the phase speed across the Tropics and has realistic amplitude. However, the period is faster than observed, consistent with the space–time spectra in Fig. 5d. This is the simulation on which we concentrate our more in-depth analysis of the MJO given the well-defined eastward propagating signal.

4. The composite life cycle of the model MJO

An MJO index is derived similar to MH98. The filtered pentad anomalies are averaged from 7°N to 7°S for both model (T_DD20) and reanalysis. Subsets are retrieved for the 15 extended winters from 1979 to 1993. Intraseasonal variations in the 850-hPa zonal wind are extracted using empirical orthogonal function analysis. EOF-1 and EOF-2 from the reanalysis and model are displayed in Fig. 8. In both model and reanalysis, the first two EOFs are significantly different from the higher order modes based on the North et al. (1982) criterion. The model (Fig. 8b) captures the quadrature relationship between the two leading EOFs over the Eastern Hemisphere, as seen in the reanalysis (Fig. 8a). Model EOF-1 has a maximum over the Indian Ocean and a minimum over the western Pacific Ocean, comparable to observations. The model EOF-2 peaks near 130°E, slightly west of the reanalysis, and to the east the amplitude decreases faster than observed. Simulated EOF-1 (EOF-2) explains comparable (slightly less) variance than observed.

The quadrature relationship between the first two EOFs is further shown by the lag correlation coefficients of the corresponding principle components (PCs: Table 2). From Table 2 we note that for the reanalysis the lag correlations for pentads 1–3 are similar, while in the model it drops dramatically at a lag of 3 pentads. This is consistent with the faster-than-observed EOF-2 amplitude decline near the date line (Fig. 8b). Consequently, we define the MJO index time series as a linear combination of the PC1 and PC2. The index for the model is defined as

$$\text{index1}(t) = \text{PC1}(t) + [\text{PC2}(t+1) + \text{PC2}(t+2)]/2, \tag{4.1}$$

and for the reanalysis as

$$\text{index2}(t) = \text{PC1}(t) + [\text{PC2}(t+1) + \text{PC2}(t+2) + \text{PC2}(t+3)]/3, \tag{4.2}$$

where t is the time in pentads.

We consider nine phases in the composite life cycle of the MJO, though only a few are shown for brevity. MJO events for compositing are selected based on a one standard deviation (STD) criterion in the index time series. The first point that is below or equal to −STD is a candidate for phase 1. Starting from this point, if the index advances to +STD or above then reverses back to −STD or below, an MJO event is selected with the starting point defined as phase 1. The maximum positive departure of the index (+STD) is denoted phase 5, and the second minima at or below −STD is phase 9. All phases of 1, 5, and 9 have to be

TABLE 2. Correlation coefficients of PC1 leading PC2 from 0 to 7 pentads during the extended winters in 1979–93.

	Lead							
	0	1	2	3	4	5	6	7
NCEP	0.00	0.31	0.43	0.37	0.19	0.00	−0.14	−0.18
T_DD20	0.00	0.53	0.53	0.16	−0.16	−0.23	−0.16	−0.07
DOF*	538	537	536	535	534	533	532	531
99%**	0.111							0.1117

* DOF = degree of freedom.
** Significance level at 99%.

included in a selected MJO event, while any other phase may be missed because the selected events have different dominant periods. A point within 0.3 × STD of zero from phases 1 to 5 is phase 3; from 5 to 9 is phase 7. The value 0.3 is used to include more samples for the transition phase. The main features are unchanged if a smaller interval is used. Any point lying between two consecutive odd-number phases is defined as a corresponding even-numbered phase. The criterion used here is relaxed such that the index does not have to be strictly increasing or decreasing; backward-moving points of 0.1 × STD are allowed, but no more than two such points can occur consecutively. After a selected MJO event, the point for phase 9 is the starting point for another potential event. There are 20 selected events in T_DD20 and 11 in the observations, while the total numbers for each phase are different. Because of our stricter criteria, including only analyzing the boreal winter, the number of observed MJO events is less than in MH98. However, the main features of the MJO remain, as will be shown in the following sections. Conventional two-tail Student's *t* tests for the difference of the anomalies from zero are conducted based on these numbers in the following plots. Bandpass-filtered winds, surface latent heat flux, convergence, and precipitation are composited for each phase. Vertically integrated water vapor from the surface to 850 hPa is also composited because it is a key component in the frictional moisture convergence mechanism (Wang and Rui 1990; MH98; Sperber 2003).

Phase 1 occurs after the onset of convection over the western equatorial Indian Ocean (Fig. 9a). The onset occurs in the presence of low-level easterly wind anomalies, and suppressed convection dominates the tropical western Pacific Ocean, consistent with the observations of Sperber (2003). The flow at 850 and 200 hPa shows that the model captures the baroclinic structure of the MJO. Convergence at 1000 hPa (Fig. 9b) and positive boundary moisture anomalies (Fig. 9c) support the convection over the western Indian Ocean. The near-equatorial moisture anomalies and convergence also occur farther eastward, suggesting preconditioning of the atmosphere in advance of the deep convection.

During phase 3 the enhanced rainfall of ~8 mm day^{-1} is located near 90°E, though it is characterized by two off-equatorial maxima (Fig. 10a). West of the precipitation weak vortices are anticyclonic at 200 hPa and cyclonic at 850 hPa off the equator. These features resemble a Rossby wave response (e.g., Gill 1980) to the precipitation (Rui and Wang 1990). It is noticed that numerous small convective centers lie near the equator from the eastern Indian Ocean to the west Pacific. As seen in Figs. 10b and 10c, the low-level convergence

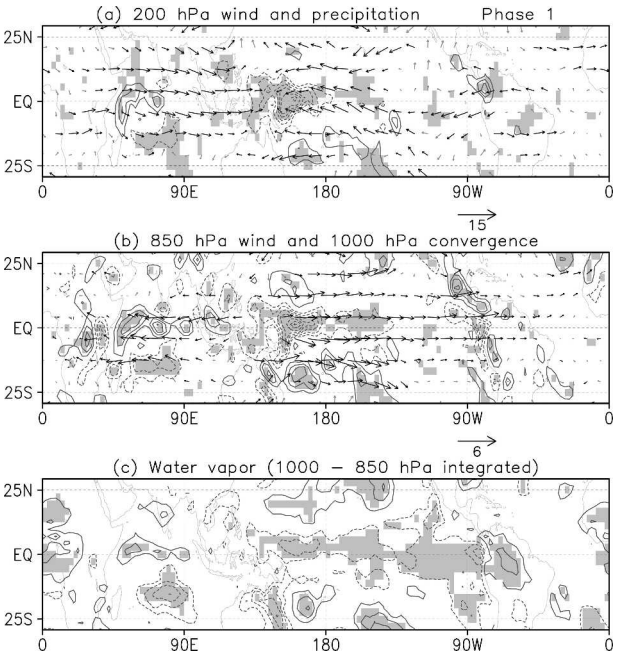

FIG. 9. Phase 1 of the composite life cycle of the MJO from T_DD20 with filtered anomalies during winter. (a) 200-hPa wind and precipitation. Interval for precipitation is 2 mm day^{-1}. (b) 850-hPa wind and 1000-hPa convergence (solid). Interval for convergence is 7×10^{-7} s^{-1}. (c) 1000–850-hPa integrated water vapor with interval of 0.5 g Kg^{-1}. Shaded and black vectors are values over a 90% confidence level of a Student's *t* test. All contour plots exclude zero. See text for the MJO index and definitions for the phases.

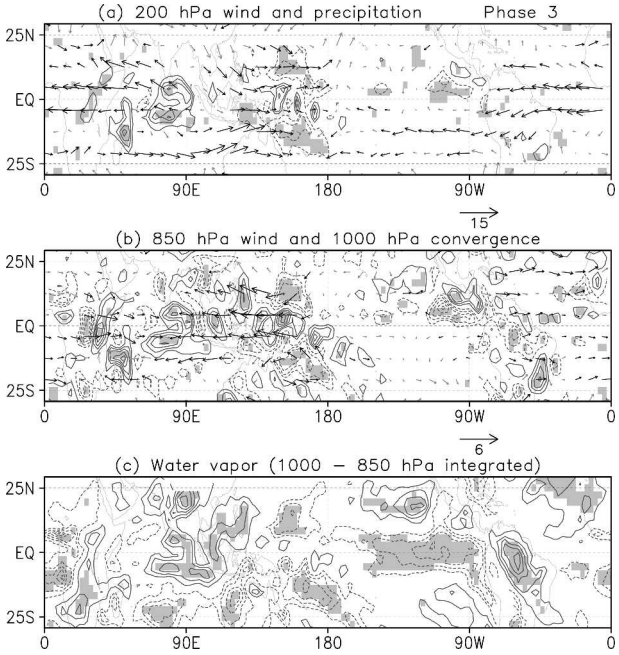

FIG. 10. As in Fig. 9, but for phase 3.

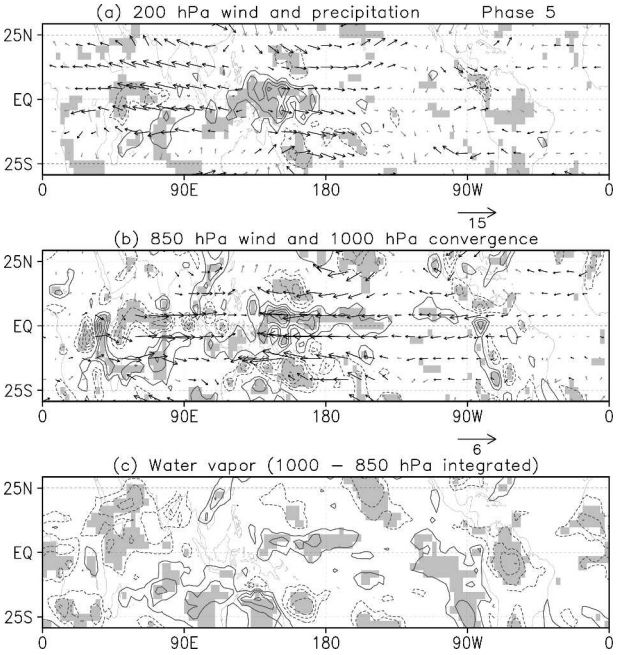

FIG. 11. As in Fig. 9, but for phase 5.

and enhanced moisture are in phase with the enhanced convection. The enhanced rainfall over the west Pacific is contrary to observations that indicate in situ suppressed convection to be prevalent (Sperber 2003).

During phase 4, positive near-equatorial rainfall anomalies extend from 90° to 160°E, and weak low-level convergence extends to the date line (not shown). However, a commensurate increase in low-level moisture near the date line is lacking. In phase 5 the equatorial rainfall extends to the date line as suppressed convection takes hold over the western Indian Ocean (Fig. 11a). The Rossby–Kelvin wave structure in winds is clearly defined and shifts eastward 60°–80° compared to phase 3 (Fig. 10a). Convergence at 1000 hPa and low-level positive moisture anomalies extend across the date line, leading the positive precipitation eastward.

During phases 6 (not shown) and 7 (Fig. 12a) the enhanced rainfall extends east of the date line and bifurcates. The Southern Hemisphere branch weakens as it migrates into the South Pacific convergence zone, and the Northern Hemisphere component, which is not typically seen in other observed studies, tends to be weaker with slight migration to the northeast.

As noted above, there are times when either, or both, the low-level convergence and enhanced moisture precede the subsequent development of convection, most notably during the transition from phase 4 to phase 6. Longitude–phase plots of anomalies of 7°N–7°S averaged precipitation and 1000-hPa convergence (Fig. 13a) and low-level moisture (Fig. 13b) indicate that weak preconditioning of the simulated atmosphere is evident from 120°E to 180°. However, there is a major discrepancy in the model, with the strongest near-surface convergence anomalies occurring in phase with the convection, unlike observations in which the convergence anomalies are in quadrature with the convection (e.g., Sperber 2003). Thus, the simulated low-level moisture

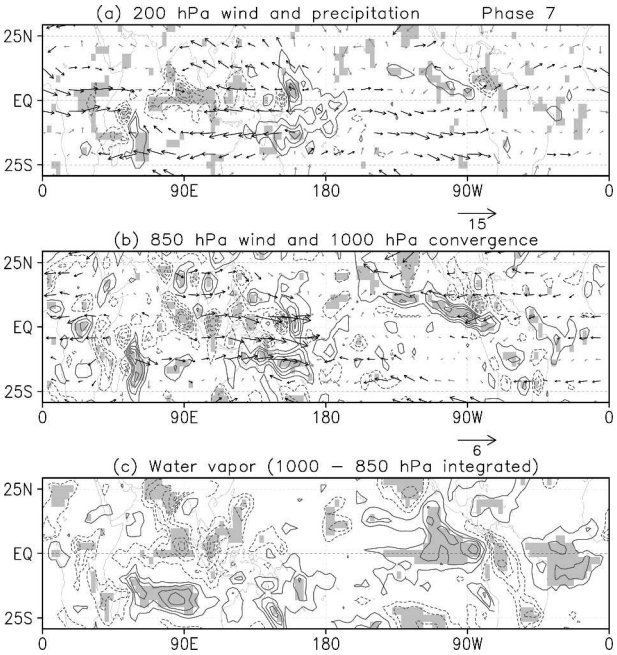

FIG. 12. As in Fig. 9, but for phase 7.

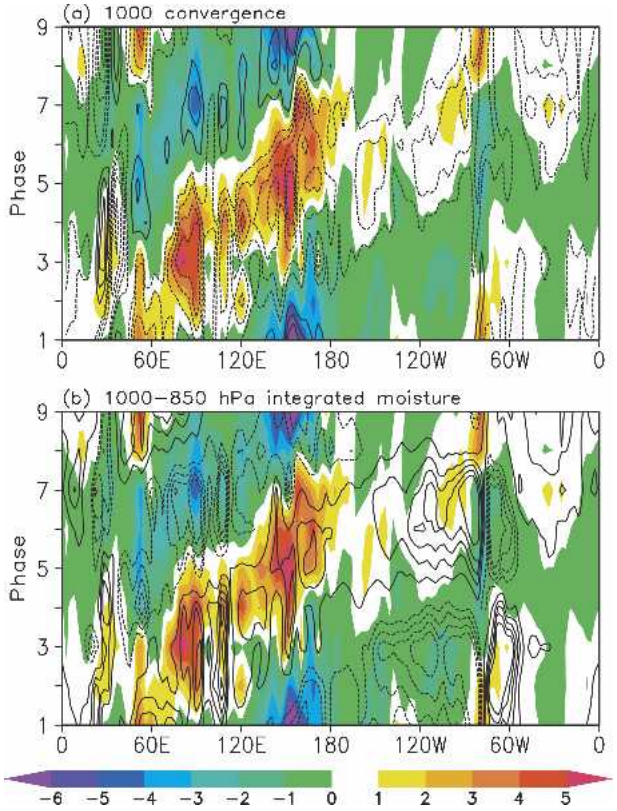

FIG. 13. Quadrature relationship of convection with (a) 1000-hPa convergence and (b) 1000–850-hPa integrated moisture during the composite life cycle of the MJO in T_DD20 based on the index in (4.2). Precipitation is color shaded with an interval of 1 mm day^{-1} excluding zero. Contour unit for convergence is 1 × 10^{-7} s^{-1} with levels of –20, −15, −10, −5, −1, 10, 15, and 20 shown. Unit for moisture is 1 g Kg^{-1} with levels of –1.5, −1.2, −0.9, −0.6, 0.2, 0.6, 0.9, 1.2, and 1.5 shown.

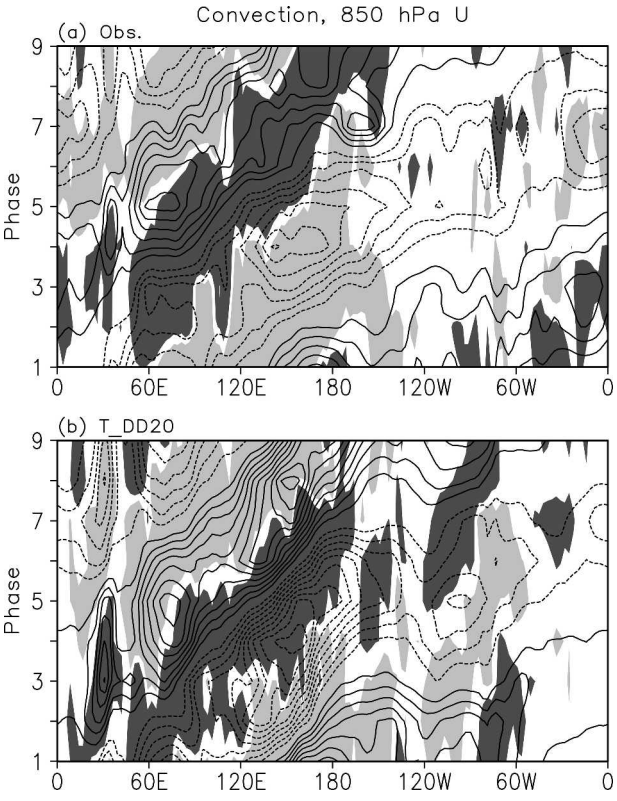

FIG. 14. Convection and 850-hPa zonal wind averaged in 7°N ~ 7°S in a composite life cycle of the MJO in (a) observation (NCEP wind and CMAP rainfall) and (b) T_DD20 based on the indices in (4.1) and (4.2). Precipitation below –0.5 mm day^{-1} and above 0.5 mm day^{-1} is shaded with dark as positive and light as negative. Contour represents wind with solid lines as westerlies and dashed lines as easterlies. Interval for winds is 0.5 m s^{-1}.

convergence is not as demonstrative as in observations.

Figure 14 indicates a systematic error in the zonal winds that was also evident in the phase composites, namely that in the model easterly anomalies at the leading edge of the convection dominate the low-level inflow (Fig. 14b), contrary to observations. In reanalysis the onset of the MJO convection occurs in an easterly basic state (Sperber 2003). However, once the convection matures over the central Indian Ocean, westerlies dominate the low-level inflow, and the low-level moisture convergence helps maintain the eastward propagation. In the model, with the systematic error of mean easterlies over the near equatorial Indian Ocean (Fig. 1d), the easterly intraseasonal anomalies give rise to enhanced evaporation at and to the east of the convection over the Indian Ocean that persists in phases 1–4 (Fig. 15), contrary to observations. This suggests that over the Indian Ocean, WISHE (Emanuel 1987; Neelin et al. 1987) dominates in the model. Over the west Pacific, the simulated latent heat flux is more consistent with observations in that convection is preceded (followed) by suppressed (enhanced) evaporation. However, the dominance of the low-level easterly inflow relative to the convection produces weak low-level moisture convergence in the model.

5. Summary and discussion

This study investigated the MJO simulated by the NCAR CAM2 with different convective parameterization schemes and different configurations of the Tiedtke (1989) convective scheme. We conducted a series of AMIP-type runs from January 1978 to March 1995 with specified monthly mean sea surface temperature (SST) and sea ice as external forcing. The standard CAM2 that retains the ZM95 scheme simulates less realistic mean state precipitation over the tropical Eastern Hemisphere and no evidence of eastward-propagating intraseasonal variability in the Tropics. This con-

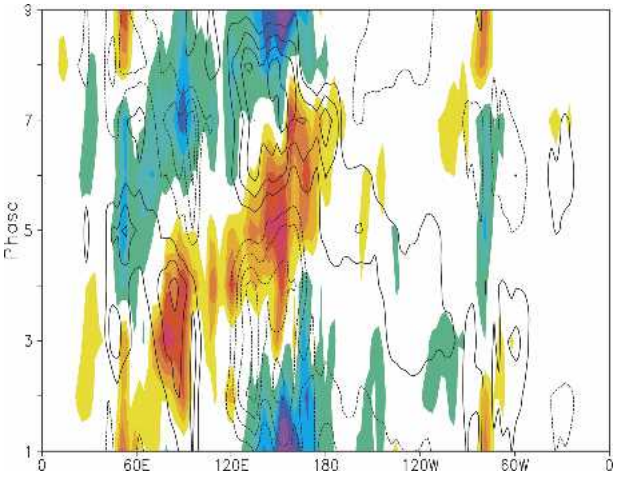

FIG. 15. As in Fig. 13 but contoured for surface latent heat flux anomalies with interval of 5 W m^{-2} starting from ± 5. Positive anomalies correspond to oceanic cooling.

firms the deficiencies noted by Sperber (2004), and those previously noted in the CCM3 (Maloney and Hartmann 2001; Maloney 2002), which also used the ZM95 scheme. Although these deficiencies in the CCM3 can be markedly reduced by an alternate scheme of McRAS, some weaknesses remain, particularly in the Indian Ocean where weaker zonal winds at 850 hPa and deficient precipitation associated with the MJO were simulated. These deficiencies can be attributed to the McRAS scheme and the perpetual March experiment design used in Maloney and Hartmann (2001).

To attempt to simulate a more realistic MJO especially over the Indian Ocean, we implemented the Tiedtke (1989) convective scheme in the CAM2. The Tiedtke scheme (T_DD20) is closed on moisture convergence, a key component in the frictional moisture convergence mechanism for the MJO. Nordeng (1994) revised the Tiedtke scheme for deep convection by changing its closure from moisture convergence to CAPE (TN_DD30), and simulations with this scheme have shown good ability to represent the Madden–Julian variability during winter (K. R. Sperber 2004, unpublished manuscript) and summer (Kemball-Cook et al. 2002; Fu et al. 2003). Our results show that the CAM2 with the Tiedtke (1989) convective schemes produces more reasonable mean states than the CTL compared to observations, particularly for precipitation. The Nordeng revised scheme (TN_DD30) enhances the simulated precipitation over the Indian–Pacific Oceans, but the amplitude is still too low in the equatorial Indian Ocean. Precipitation from the Tiedtke scheme (T_DD20) is the closest to observations with more realistic amplitude.

Intraseasonal-filtered precipitation shows similar advantages and deficiencies in the CAM2 runs as in the mean state. Generally, the T_DD20 simulates the best agreement in spatial distribution with the observations except that it has somewhat larger amplitude. Coinciding with previous studies, the observational data show that the MJO has more eastward propagation than westward and power concentrated in zonal wavenumbers 1–3 for periods of 30–70 days. The CTL run does not represent these features. The TN_DD30 simulates an MJO with about half of the power in zonal wind that is seen in observations and very weak power in precipitation, indicating weak coherence among the dynamical and convective fields. The T_DD20 produces most of the observed features, especially over the western-central Pacific Ocean, with comparable amplitude to the observations except that the dominant period also has a maximum near 30 days during the winter. In the CAM2 model the comparison between the TN_DD30 and T_DD20 indicates that the Tiedtke convective scheme closed on moisture convergence produces a better MJO than the scheme closed on moist static energy, contrary to the suggestion of Slingo et al. (1996). Even though such a suggestion can be deduced from examination of a large number of models, our results indicate that applicability must be tested on a model by model basis.

A composite life cycle of the simulated MJO shows a more regular structure in the Eastern Hemisphere, and the frictional convergence mechanism is more apparent than in the CAM2 control run. The MJO initializes in the western Pacific and moves slowly eastward. A forced Rossby–Kelvin wave structure is clearly displayed in dynamical fields that move eastward with the convection. Despite the pronounced improvement in tropical eastward intraseasonal variability, the model displays two mechanisms for maintaining eastward propagation. With the easterly bias over the Indian Ocean in the time mean state, low-level easterly intraseasonal anomalies give rise to increased evaporation with wind-induced surface heat exchange modulating the propagation. Over the western and central Pacific Ocean low-level convergence and moisture anomalies lead convection by 1–2 pentads, enabling moisture preconditioning and the buildup of moist static energy. However, these leading anomalies are weaker than observed and, contrary to observations, the strongest anomalies are more closely in phase with the convection. As a consequence, easterly anomalies tend to dominate the low-level inflow to the convection in the model. Similar to observations, the dynamical signal radiates eastward at a faster phase speed once the intraseasonal convection ceases near the date line.

Sensitivity experiments with the Tiedtke convective scheme show that enhancing the downdrafts significantly shifts the MJO to shorter periods and reduces the MJO power, but to a lesser extent than if the scheme is closed on CAPE. Other features of the MJO remain unchanged, which is in agreement with previous studies.

In CAM2 the Tiedtke (1989) scheme closed on moisture convergence simulates a better MJO than when it is closed on CAPE, although the same advantage does not occur in the ECHAM4 model that includes the Nordeng closure (not shown). Consequently, it cannot be concluded that the moisture closure of the Tiedtke scheme is superior to the CAPE closure. Other moist and diabatic processes in the CAM2 model may also contribute to the improvement of the MJO simulation when the Tiedtke convective scheme is implemented, including the interaction of convection with the boundary layer scheme. The Zhang and McFarlane (1995) scheme produces a reasonable mean state particularly in 850-hPa zonal wind. Why this scheme does not produce a realistic MJO structure is an interesting issue that deserves further investigation. To understand the reason will further advance the understanding of MJO in the simulation.

In these experiments we have neglected air–sea interaction since we specified the observed SST as a boundary condition. Since air–sea interaction has usually been shown to improve the representation of the MJO (Inness and Slingo 2003; Sperber 2004), we plan to repeat these experiments with the atmospheric model coupled to an ocean model.

Acknowledgments. This research was partially supported by the Japan Agency for Marine-Earth Science and Technology (JAMSTEC) through its sponsorship of the International Pacific Research Center. We thank Dr. Erik Roeckner for providing the Tiedtke convective scheme included in the ECHAM4.6. We thank CDC for providing the NCEP–NCAR reanalysis data. K. R. Sperber was supported by the U.S. Department of Energy, Office of Science Climate Change Prediction Program, at the University of California Lawrence Livermore National Laboratory under Contract W-7405-ENG-48. B. Wang and T. Li acknowledge the support from NSF Climate Dynamics Program ATM-0329531 and ONR Grant N000140310739.

REFERENCES

Arakawa, A., and W. H. Schubert, 1974: Interaction of a cumulus cloud ensemble with the large-scale environment. Part I. *J. Atmos. Sci.,* **31,** 674–701.

Bladé, I., and D. L. Hartmann, 1993: Tropical intraseasonal oscillations in a simple nonlinear model. *J. Atmos. Sci.,* **50,** 2922–2939.

Chao, W. C., and S.-J. Lin, 1994: Tropical intraseasonal oscillation, super cloud clusters, and cumulus convection schemes. *J. Atmos. Sci.,* **51,** 1282–1297.

——, and L. Deng, 1998: Tropical intraseasonal oscillation, super cloud clusters, and cumulus convection schemes. Part II: 3D aquaplanet simulations. *J. Atmos. Sci.,* **55,** 690–709.

Emanuel, K. A., 1987: An air–sea interaction model of intraseasonal oscillation in the Tropics. *J. Atmos. Sci.,* **44,** 2324–2340.

Fu, X., B. Wang, T. Li, and J. P. McCreary, 2003: Coupling between northward-propagating, intraseasonal oscillations and sea surface temperature in the Indian Ocean. *J. Atmos. Sci.,* **60,** 1733–1753.

Gates, W. L., 1992: AMIP: The Atmospheric Model Intercomparison Project. *Bull. Amer. Meteor. Soc.,* **73,** 1962–1970.

Gill, A. E., 1980: Some simple solutions for heat-induced tropical circulation. *Quart. J. Roy. Meteor. Soc.,* **106,** 447–462.

Gualdi, S., A. Navarra, and G. Tinarelli, 1999: The interannual variability of the Madden–Julian oscillation in an ensemble of GCM simulations. *Climate Dyn.,* **15,** 643–658.

Hack, J. J., 1994: Parameterization of moist convection in the National Center for Atmospheric Research Community Climate Model (CCM2). *J. Geophys. Res.,* **99,** 5551–5568.

Hendon, H. H., 2000: Impact of air–sea coupling on the Madden–Julian oscillation in a general circulation model. *J. Atmos. Sci.,* **57,** 3939–3952.

——, and B. Liebmann, 1990: The intraseasonal (30–50 day) oscillation of the Australian summer monsoon. *J. Atmos. Sci.,* **47,** 2909–2924.

——, and M. L. Salby, 1994: The life cycle of the Madden–Julian oscillation. *J. Atmos. Sci.,* **51,** 2225–2237.

Hu, Q., and D. A. Randall, 1994: Low-frequency oscillations in radiative–convective systems. *J. Atmos. Sci.,* **51,** 1089–1099.

Inness, P. M., and D. Gregory, 1997: Aspects of the intraseasonal oscillation simulated by the Hadley Centre Atmosphere Model. *Climate Dyn.,* **13,** 441–458.

——, and J. M. Slingo, 2003: Simulation of the Madden–Julian oscillation in a coupled general circulation model. Part I: Comparison with observations and an atmosphere-only GCM. *J. Climate,* **16,** 345–364.

——, and Coauthors, 2003: Simulation of the Madden–Julian oscillation in a coupled general circulation model. Part II: The role of the basic state. *J. Climate,* **16,** 365–382.

Jones, C., and B. C. Weare, 1996: The role of low-level moisture convergence and ocean latent heat fluxes in the Madden–Julian oscillation: An observational analysis using ISCCP data and ECMWF analyses. *J. Climate,* **9,** 3086–3104.

Kalnay, E., and Coauthors, 1996: The NCEP/NCAR 40-Year Reanalysis Project. *Bull. Amer. Meteor. Soc.,* **77,** 437–471.

Kemball-Cook, S., B. Wang, and X. Fu, 2002: Simulation of the intraseasonal oscillation in ECHAM4 model: The impact of coupling with an ocean model. *J. Atmos. Sci.,* **59,** 1433–1453.

Kiehl, J. T., J. J. Hack, and J. W. Hurrell, 1998: The National Center for Atmospheric Research Community Climate Model: CCM3. *J. Climate,* **11,** 1131–1150.

Kuo, H.-L., 1974: Further studies of the parameterization of the influence of cumulus convection on large-scale flow. *J. Atmos. Sci.,* **31,** 1232–1240.

Lee, M.-I., I.-S. Kang, and B. E. Mapes, 2003: Impacts of cumulus convection parameterization on aqua-planet AGCM simulations of tropical intraseasonal variability. *J. Meteor. Soc. Japan,* **81,** 963–992.

Madden, R. A., and P. R. Julian, 1971: Detection of a 40–50 day oscillation in the zonal wind in the tropical Pacific. *J. Atmos. Sci.,* **28,** 702–708.

——, and ——, 1972: Description of global-scale circulation cells in the Tropics with a 40–50 day period. *J. Atmos. Sci.,* **29,** 1109–1123.

——, and ——, 1994: Observations of the 40–50-day tropical oscillation—A review. *Mon. Wea. Rev.,* **122,** 814–837.

Maloney, E. D., 2002: An intraseasonal oscillation composite life cycle in the NCAR CCM3.6 with modified convection. *J. Climate,* **15,** 964–982.

——, and D. L. Hartmann, 1998: Frictional moisture convergence in a composite life cycle of the Madden–Julian oscillation. *J. Climate,* **11,** 2387–2403.

——, and ——, 2001: The sensitivity of intraseasonal variability in the NCAR CCM3 to changes in convective parameterization. *J. Climate,* **14,** 2015–2034.

Manabe, S., J. Smagorinsky, and R. F. Strickler, 1965: Simulated climatology of a general circulation model with a hydrological cycle. *Mon. Wea. Rev.,* **93,** 769–798.

Meehl, G. A., G. N. Kiladis, K. M. Weickmann, M. Wheeler, D. S. Gutzler, and G. P. Compo, 1996: Modulation of equatorial subseasonal convective episodes by tropical–extratropical interaction in the Indian and Pacific Ocean regions. *J. Geophys. Res.,* **101,** 15 033–15 049.

——, R. Lukas, G. N. Kiladis, K. M. Weickmann, A. J. Matthews, and M. Wheeler, 2001: A conceptual framework for time and space scale interactions in the climate system. *Climate Dyn.,* **17,** 753–775.

Moorthi, S., and M. J. Suarez, 1992: Relaxed Arakawa–Schubert: A parameterization of moist convection for general circulation models. *Mon. Wea. Rev.,* **120,** 978–1002.

Neale, R., and J. Slingo, 2003: The Maritime Continent and its role in the global climate: A GCM study. *J. Climate,* **16,** 834–848.

Neelin, J. D., I. M. Held, and K. H. Cook, 1987: Evaporation wind feedback and low-frequency variability in the tropical atmosphere. *J. Atmos. Sci.,* **44,** 2341–2348.

Nordeng, T. E., 1994: Extended versions of the convective parameterization scheme at ECMWF and their impact on the mean and transient activity of the model in the Tropics. ECMWF Tech. Memo. 206, 41 pp.

North, G. R., T. L. Bell, R. F. Cahalan, and F. J. Moeng, 1982: Sampling errors in the estimation of empirical orthogonal functions. *Mon. Wea. Rev.,* **110,** 699–706.

Park, C. K., D. M. Straus, and K. M. Lau, 1990: An evaluation of the structure of tropical intraseasonal oscillations in three general circulation models. *J. Meteor. Soc. Japan,* **68,** 403–417.

Rasch, P. J., and J. E. Kristjánsson, 1998: A comparison of the CCM3 model climate using diagnosed and predicted condensate parameterizations. *J. Climate,* **11,** 1587–1614.

Roeckner, E., and Coauthors, 1996: The atmospheric general circulation model ECHAM-4: Model description and simulation of present-day climate. Max Planck Institute for Meteorology Rep. 218, 90 pp.

Rui, H., and B. Wang, 1990: Development characteristics and dynamic structure of tropical intraseasonal convection anomalies. *J. Atmos. Sci.,* **47,** 357–379.

Salby, M. L., and H. H. Hendon, 1994: Intraseasonal behavior of clouds, temperature, and motion in the Tropics. *J. Atmos. Sci.,* **51,** 2207–2224.

Sheng, J., 1995: The Madden–Julian oscillation in the Canadian Climate Centre general circulation model. *Climate Dyn.,* **12,** 125–140.

Slingo, J. M., and Coauthors, 1996: Intraseasonal oscillation in 15 atmospheric general circulation models: Results from an AMIP diagnostic subproject. *Climate Dyn.,* **12,** 325–357.

Sperber, K. R., 2003: Propagation and the vertical structure of the Madden–Julian oscillation. *Mon. Wea. Rev.,* **131,** 3018–3037.

——, 2004: Madden–Julian variability in NCAR CAM2 and CCSM2. *Climate Dyn.,* **23,** 259–278.

Sud, Y. C., and G. K. Walker, 1999: Microphysics of clouds with the relaxed Arakawa–Schubert Scheme (McRAS). Part I: Design and evaluation with GATE phase III data. *J. Atmos. Sci.,* **56,** 3196–3220.

Sundqvist, H., 1988: Parameterization of condensation and associated clouds in models for weather prediction and general circulation simulation. *Physically-Based Modeling and Simulation of Climate and Climate Change*, M. E. Schlesinger, Ed., Vol. 1, Kluwer Academic, 433–461.

Tiedtke, M., 1989: A comprehensive mass flux scheme for cumulus parameterization in large-scale models. *Mon. Wea. Rev.,* **117,** 1779–1800.

Wang, B., and H. Rui, 1990: Dynamics of the coupled moist Kelvin–Rossby wave on an equatorial β-plane. *J. Atmos. Sci.,* **47,** 397–413.

Wang, W., and M. E. Schlesinger, 1999: The dependence on convection parameterization of the tropical intraseasonal oscillation simulated by the UIUC 11-layer atmospheric GCM. *J. Climate,* **12,** 1423–1457.

Williamson, D. L., and J. G. Olson, 2003: Dependence of aquaplanet simulations on time step. *Quart. J. Roy. Meteor. Soc.,* **129,** 2049–2064.

Woolnough, S. J., J. M. Slingo, and B. J. Hoskins, 2000: The relationship between convection and sea surface temperature on intraseasonal timescales. *J. Climate,* **13,** 2086–2104.

Xie, P., and P. A. Arkin, 1997: Global precipitation: A 17-year monthly analysis based on gauge observations, satellite estimates, and numerical model outputs. *Bull. Amer. Meteor. Soc.,* **78,** 2539–2558.

Zhang, G. J., and N. A. McFarlane, 1995: Sensitivity of climate simulations to the parameterization of cumulus convection in the Canadian Climate Centre general circulation model. *Atmos.–Ocean,* **33,** 407–446.

Zhang, M., and Coauthors, 2003: A modified formulation of fractional stratiform condensation rate in the NCAR community atmospheric model (CAM2). *J. Geophys. Res.,* **108,** 4035, doi:10.1029/2002JD002523.